

# Soliton crystals in Kerr resonators

Daniel C. Cole<sup>1,2</sup>, Erin S. Lamb<sup>1</sup>, Pascal Del’Haye<sup>1,3</sup>, Scott A. Diddams<sup>1</sup>, and Scott B. Papp<sup>1</sup>

<sup>1</sup>*National Institute of Standards and Technology (NIST), Boulder, CO 80305, USA*

<sup>2</sup>*Department of Physics, University of Colorado, Boulder, CO 80309, USA*

<sup>3</sup>*Present address: National Physical Laboratory (NPL), Teddington, TW11 0LW, United Kingdom*

Corresponding author: [daniel.cole@nist.gov](mailto:daniel.cole@nist.gov)

**Solitons<sup>1</sup> are pulses that propagate without spreading due to a balance between nonlinearity and dispersion (or diffraction), and are universal features of systems exhibiting these effects. Solitons play an important role in plasma physics<sup>2</sup>, fluid dynamics<sup>3</sup>, atomic physics<sup>4</sup>, biology<sup>5</sup>, and optics<sup>6–10</sup>. In the context of integrated photonics, bright dissipative cavity solitons in Kerr-nonlinear resonators<sup>11–14</sup> are envisioned to play an important role in next-generation communication, computation, and measurement systems<sup>15–17</sup>. Here we report the discovery of soliton crystals in Kerr resonators—collectively ordered ensembles of co-propagating solitons with discrete allowed temporal separations. Through analysis of optical spectra, we identify a complicated but discrete space of interacting soliton configurations, including crystals exhibiting vacancies (Schottky defects), shifted pulses (Frenkel defects), and superstructure. Time-domain characterization of the output-coupled soliton pulse train directly confirms our inference of the crystal configuration. The soliton crystals’ optical spectra also reveal the mechanism that stabilizes them. Excess optical power on a particular comb mode arises from perturbations to resonator mode frequency, and in the time-domain, creates an extended traveling wave that counterbalances attractive soliton interactions. Thus, soliton crystals are a new class of nonlinear wave eigenstates balanced by nonlinearity, dispersion, and long-range soliton interactions. Our work explores the rich physics of nonlinear Kerr resonators and offers a chip-based, low-power source of femtosecond soliton pulse trains at 400 GHz for frequency synthesis and waveform generation in optical and millimeter-wave communications, and other applications. More broadly, it reveals a mechanism for collective soliton interactions in nonlinear systems through a perturbation to dispersion or diffraction.**

Optical solitons have recently found a new realization in frequency combs generated in Kerr-nonlinear resonators<sup>15</sup>. Kerr combs are a major step forward in frequency comb technology<sup>18</sup> because they enable generation of frequency combs in platforms having low size, weight, and power requirements. When a continuous-wave pump laser is coupled into a whispering-gallery mode of a high-Q Kerr resonator, broad optical spectra are generated through cascaded four-wave mixing. With appropriate power and laser-resonator frequency detuning, the resulting fields may mode-lock to form circulating dissipative cavity solitons<sup>11,19</sup>. These solitons are excitations with robust, deterministic properties that may be tailored through resonator design<sup>20,21</sup> and tuned in real-time through manipulation of the pump laser. Kerr frequency combs extend the range of accessible comb repetition rates and provide a route towards chip-integrated self-referenced comb technology.

Single solitons and ensembles of co-propagating solitons have been reported in Kerr resonators constructed from a variety of crystalline and amorphous materials<sup>11–14,22</sup>, with repetition frequencies ranging from 22 GHz<sup>14</sup> to 1 THz<sup>22</sup>. Co-propagating Kerr solitons exhibit attractive interactions culminating mostly in pair-annihilation; it is possibly for this reason that so far only sparsely populated soliton ensembles have been observed in experiments. In contrast, in this Letter we report on the generation of tightly packed, strongly interacting, yet stable Kerr-soliton crystal ensembles, which exhibit novel collective temporal ordering. Crystallization of Kerr solitons manifests in our experiments with distinctive optical spectra precisely related to spectral interference between interacting solitons, and as soliton pulse trains with discrete temporal spacings measured through ultrafast cross-correlation techniques. A series of physical effects supported by the resonator itself is responsible for Kerr crystals. First, since the solitons are

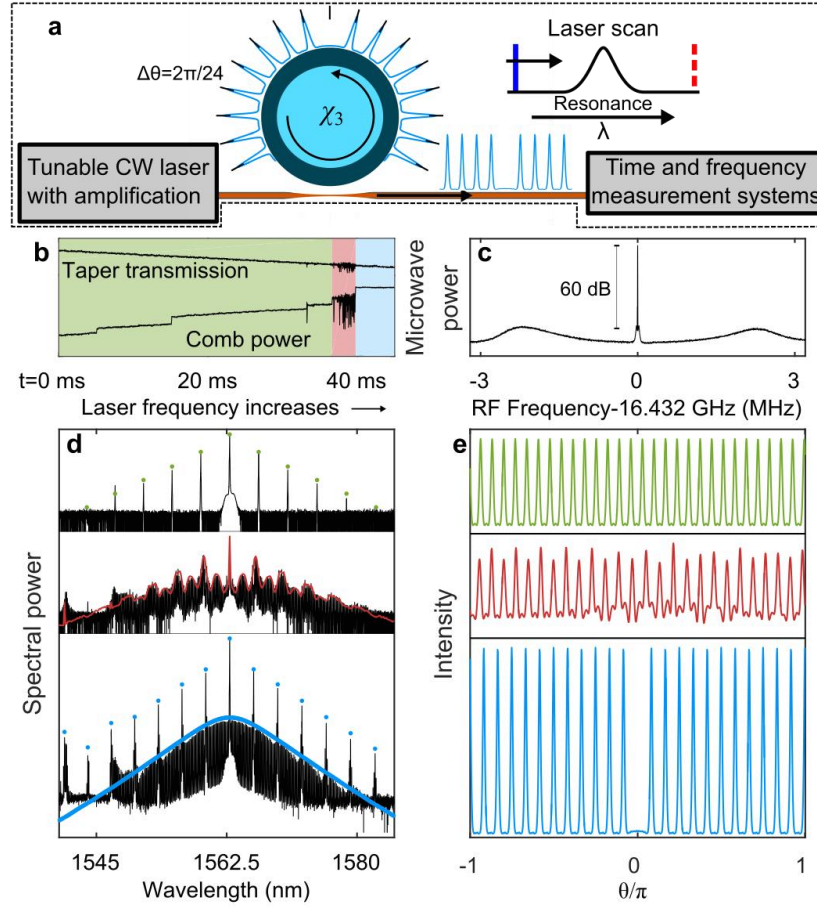


Figure 1. Generation of a soliton crystal using the Kerr nonlinearity in a  $\chi_3$ -nonlinear medium (here silica). (a) Depiction of generation and measurement of a crystal. The laser scan across the resonance from blue laser detuning to red laser detuning is shown schematically. (b) Taper transmission and comb power during crystal generation. A thermal shift of the resonance leads to the non-Lorentzian taper transmission profile. Three regimes are visible: primary comb (green), chaos (red), and crystal (blue). (c) Narrow measured RF beat indicating crystallization. (d) Progression of experimental optical spectra (black) through the three regimes, with simulations (color). Range of each plot is 100 dB. (e) Simulated time-domain waveforms corresponding to the optical spectra plotted in (d), plotted against the angular coordinate in a co-rotating frame (arbitrary vertical scale).

tightly packed, a Kerr crystal has intracavity optical power similar to that of its precursor, a time-varying chaotic intracavity waveform arising from modulation instability<sup>11,19</sup>. Hence, crystals form through adiabatic pump-laser frequency scans, without the complex techniques employed in other demonstrations of Kerr solitons. Second, destructive soliton collisions are eliminated through the automatic formation of an extended background wave in the cavity that counterbalances attractive interactions. This happens because resonator mode-family degeneracies locally enhance (or suppress) Kerr-comb formation, and interference of this excess light with the pump laser forms the extended wave that spontaneously orders tightly packed soliton ensembles. Our observations confirm the formation and characteristics of Kerr crystals. Moreover, they reveal a novel universal mechanism for soliton interactions in nonlinear systems through a perturbation to dispersion that dramatically modifies the correlation function of a soliton ensemble.

We generate soliton crystals in silica Kerr resonators with free spectral ranges (FSR) of  $\sim 26$  GHz and  $\sim 16.4$  GHz. Our experimental procedure is depicted in Fig 1a. A tapered optical fiber provides evanescent coupling of a  $\sim 30$  mW telecommunications-band pump laser into a resonator whispering-gallery mode, and also out-couples the generated Kerr-soliton-crystal frequency comb. Emerging from the resonator is a pulse train with highly ordered inter-pulse timings, which we explore in detail throughout the remainder of this paper. We form this Kerr-soliton crystal by way

of a slowly decreasing pump laser frequency scan from ‘blue’ to ‘red’ laser-cavity detuning that terminates after the soliton comb has been initiated<sup>11</sup>. This is similar to the experimental procedure that we reported previously in generation and characterization of phase-locked microcombs<sup>23,24</sup>.

To explore the process of Kerr-soliton crystal formation, we record the optical power transmitted through the tapered fiber during the laser frequency scan; see Fig. 1b. By optical filtering of the pump-laser frequency, we also measure the intensity of new comb light generated by four-wave mixing. The characteristic sawtooth shape of the resonance, contrasted with the Lorentzian profile shown in Fig. 1a, is due to thermal bistability effects<sup>25</sup>. Three qualitatively different regimes can be identified in these traces: 1. Formation of initial “primary comb”<sup>26</sup>; 2. The chaotic waveform preceding the crystal; and 3. The Kerr soliton crystal. The continuity or near continuity of the taper transmission during the transition from chaos to crystal contrasts with the dramatic “soliton steps” that have been previously reported<sup>11,14</sup>, and indicates that the intracavity optical power of the crystal is similar to that of the chaos. We observe behavior consistent with a low-noise frequency comb following transition to the Kerr crystal not only through the taper transmission and comb-power signals, but also in the microwave repetition frequency signal obtained by photodetection of the entire comb; see Fig. 1c.

The most striking aspect of Kerr crystals is their optical spectra, which feature dramatic line-by-line intensity variations due to multiple-soliton interference. Figure 1d presents measurements (black traces) delineating a particular progression from primary comb to chaotic comb to crystal for the crystal in the bottom panel, which is composed of a train of 24 solitons evenly separated in time with a single vacancy. Here the optical spectrum can be understood as the destructive interference between a tightly-packed train of 24 solitons circulating the cavity, which yields the prominent comb lines spaced by 24 resonator FSR, and a single, out-of-phase soliton that both “fills in” the spectrum and produces the vacancy in the time domain. We model these spectra to obtain predictions for their intracavity intensity pattern (Fig. 1e) using the spatio-temporal Lugiato-Lefever equation<sup>19</sup> (LLE). The numerical results, color-coded to indicate the primary comb, chaotic, and crystal regimes, are highly accurate as seen through agreement over the wide logarithmic scale variations of the spectra. While both single solitons and few-soliton ensembles are steady-state solutions to the LLE, the 23 soliton crystal in Fig. 1d is not—when it is evolved under the LLE the solitons exhibit attractive interactions and pair-wise annihilation (see Supplement). In fact, none of the crystals we present in this Letter are stable solutions of the LLE, but they are solutions to a perturbed LLE with an altered dispersion term, as described below.

The key to understanding why soliton crystals exist can be seen in their spectra. We observe excess Kerr comb generation, e.g. 6 dB near 1547 nm and 18 dB near 1541 nm in Fig. 1d, due to accidental degeneracies of the resonator mode family that supports our combs and other mode families. Such mode crossings lead to a dispersive change in the comb-resonator frequency detuning about the crossing, either increasing or decreasing the efficiency of comb formation. Mode crossing phenomena have been reported previously<sup>12,14</sup>, particularly from the standpoint of inhibiting Kerr solitons. However, mode crossings play a critical role in stabilizing attractive interactions between tightly packed, multiple-soliton ensembles. Formally the result of a mode crossing is an extended wave incorporated into the soliton waveform circulating in the resonator, which corresponds to the interference of excess light with the pump laser. When several of these perturbed solitons co-propagate in a resonator, they interact through their extended waves and arrange themselves such that the waves constructively interfere. Each soliton then lies at the peak of an extended background wave in the resonator, similar to predictions for bi-chromatically pumped Kerr combs<sup>27</sup>. Importantly, temporal separations between solitons are therefore required to be multiples of this wave’s period, the wave stabilizes the crystal against the attractive interactions discussed above, and its strength increases with the number of co-propagating perturbed solitons.

As one specific example of spontaneous crystallization driven by the extended background wave, the spectrum in the bottom of Fig. 1d exhibits excess power near optical modes  $5 \times 24=120$  (1547 nm) and  $7 \times 24=168$  (1541 nm), counted from the pump laser. Also visible is suppressed comb generation where the comb-resonator detuning has been increased. Here 24 FSR is the spacing of the prominent primary-comb lines arising from the modulation

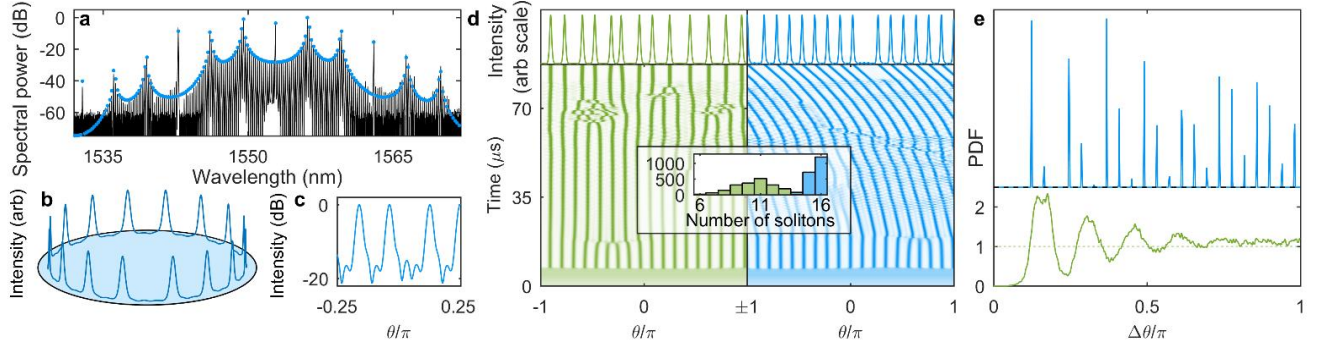


Figure 2. Investigation of a superstructured crystal. (a) Experimental (black) and simulated (blue) optical spectra. (b, c) Time-domain power of 16 nearly-uniformly distributed solitons, corresponding to the simulated spectrum in (a), on linear (b) and logarithmic (c) scales. (d) Bottom: Plots of the simulated intracavity power during a scan across the resonance, without (green) and with (blue) a mode crossing. Top: Final waveforms. Inset: Histogram of the number of solitons generated in 2000 simulated scans. (e) Average pair-distribution functions for 2000 scans across the resonance with (blue) and without (green) a mode crossing. The width of the peaks in the discrete pair-distribution function is a single  $\Delta\theta$  bin.

instability phase-matching condition, and 24 is approximately the maximum number of soliton pulses that can be seeded into the resonator. A phenomenological application of coupled-mode theory<sup>28</sup> could be employed to calculate the spectrum of the solitons perturbed by the mode crossing, but we find that to explain the stability of this 23 soliton crystal, and the apparently exact circumferential spacing of the pulses by  $2\pi/24$  radians, it is sufficient to incorporate into the LLE a reduced comb-resonator detuning on only mode 120 or on mode 168, where the excess power is largest. Then the crystal is a steady-state solution of the resulting perturbed LLE.

With the above understanding of soliton crystallization in place, we can consider a range of crystal configurations that can be explained through this universal model. To begin, we consider a second crystal spectrum, shown in Fig. 2, which was first reported by Del’Haye et al<sup>24</sup>. This crystal exhibits superstructure—the soliton train is nearly periodic in a small unit cell but is modulated with a larger periodicity. This results from the frustrated uniform distribution of 16 solitons with allowed inter-soliton separations of  $2\pi n/49$  radians; two solitons are spaced by  $4 \times 2\pi/49$  instead of  $3 \times 2\pi/49$  radians. Excess power is apparent in the spectrum at mode 49 ( $\sim 1542$  nm), and we simulate this crystal by phenomenologically reducing the comb-resonator detuning on mode 49 so that the experimental and simulated spectra agree. The background wave resulting from the constructive interference of the extended waves of the solitons, each having an angular period of  $2\pi/49$ , is visible in the plots of the simulated intensity in Figs. 2b and 2c.

To gain insight into crystal generation, we simulate laser frequency scans across the resonance that generate this crystal in the presence of the mode crossing on mode 49. Example scans are shown for the case without the mode crossing (green) and with it (blue) in Fig. 2d. In both scans, solitons emerge from chaos as the frequency of the laser is decreased. In the presence of the mode crossing, they are generated with inter-soliton separations of  $2\pi n/49$  radians. A greater number of solitons emerge from chaos in the presence of the mode crossing, and this higher number helps to stabilize the crystal against thermal changes in the experiment. Further, upon continuation of the simulation, some of the solitons in the scan without the mode crossing interact attractively and pair-annihilate, while the crystallized ensemble resulting from the scan with the mode crossing remains stable indefinitely.

We investigate the pair-distribution function (PDF) for the soliton ensembles generated by these scans. The PDF is the probability that a soliton exists at position  $\theta_o + \Delta\theta$  given that a different soliton exists at position  $\theta_o$ , normalized to the density. We note that for numerically calculated discrete PDFs the absolute scaling of the PDF is not important. In Fig. 2d, we plot the average PDFs for 2000 simulated scans with and without the mode crossing. The result for the case with a mode crossing is sharply peaked, indicating that the allowed inter-soliton separations take on discrete values. The result for the case without the mode crossing is continuous, with a peak near the most likely nearest-neighbor separation and periodic revivals at its multiples, falling to the value of the PDF for uncorrelated soliton positions at large separations. This resembles the PDF of a liquid, in contrast with that of a crystal.



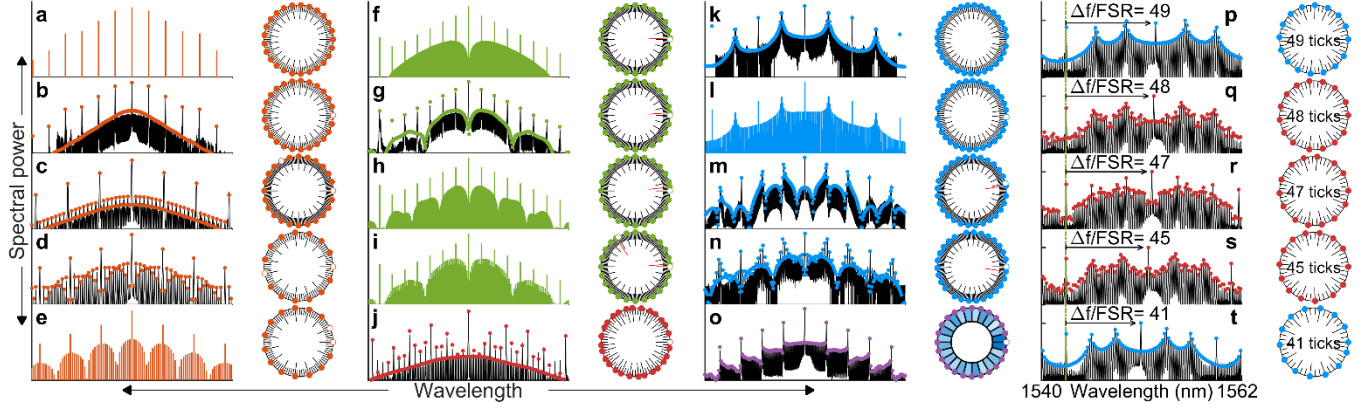


Figure 3. A taxonomy of soliton crystals. Measured optical spectra are shown in black, simulations are shown in color. Schematic depictions of the soliton distribution in the resonator are shown to the right of each spectrum. Major ticks in the schematic diagram indicate the location or expected location of a soliton. Minor ticks indicate peaks of the extended background wave due to the mode crossing. (a) A perfect soliton crystal, consisting of 25 uniformly-distributed solitons. (b-e) Soliton crystals exhibiting vacancies. (f-i) Soliton crystals exhibiting Frenkel defects. Shifted solitons still lie at peaks of the extended background wave. (j) A disordered crystal. (k-n) Crystals exhibiting superstructure. (o) A crystal with irregular inter-soliton spacings. Darker shading indicates a smaller inter-soliton spacing. The range in inter-soliton spacings is 3 % of the mean. (p-t) A series of crystals generated as the pump laser is moved progressively closer to the stabilizing mode crossing.

We observe a rich variety of soliton crystals that correspond to multiple-soliton configurations ordered according to an extended background wave; see the optical spectra plotted in Fig. 3. Operationally, we adjust the pump laser power to provide repeatable conditions for creating particular crystals. These crystals exhibit vacancies (Schottky defects), Frenkel defects, disorder, or superstructure, or some combination thereof. A Frenkel defect consists of the shifting of a soliton in an otherwise uniform crystal. Disordered crystals are crystals in which the solitons fall on the peaks of the extended background wave, but their distribution across these peaks varies without any apparent regular order or favored period.

We highlight the crystal plotted in Fig. 3n. This crystal exhibits both superstructure, with a superlattice period of  $2\pi/3$  radians, and a Frenkel defect. Three identical supercells per resonator round-trip yield a spectrum which has light in optical modes spaced by three resonator FSR, because the waveform's period has been reduced threefold. The Frenkel defect, occurring once per round-trip, contributes the single-FSR lobes to the spectrum. The result is three bursts of 8, 9, and 10 solitons respectively.

Fig. 3o shows a soliton crystal with inter-soliton separations that are slightly irregular and which we have not simulated as a steady-state solution of any perturbed LLE. We expect that the stability of the crystal and the distribution of solitons are determined by mode-interactions, but that in this case our simple approximation of a perturbation to the LLE by a reduced comb-resonator detuning on a single comb mode is not appropriate.

It is recognized in ultrafast optics that it is not generally possible to infer the time-domain waveform of an optical signal from its power spectrum without additional information<sup>29</sup>. So far in this paper we have assumed that the time-domain waveform must be a superposition of solitons, as this is a fundamental nonlinear-wave solution for Kerr combs. We can confirm this interpretation of the spectral data by performing intensity cross-correlation measurements between the soliton crystals and a single reference pulse; here we show a representative measurement for crystal 3j. For details see the Methods.

In Fig. 4, we plot the simulated time-domain waveforms of the reference pulse and the crystal (panel a), the simulated and measured cross-correlation signals (panel b), and the temporal spacing between peaks of the cross-correlation signals (panel c). We observe agreement between the measured and simulated cross-correlation signals, confirming both our generic interpretation of the spectrum as a superposition of solitons and the specific inversion of this spectrum to determine the distribution of the solitons in this disordered crystal. Beyond confirming our

interpretation of the data, the cross-correlation measurement represents the incorporation of a completely new tool into the repertoire of techniques available for investigating Kerr combs.

Soliton crystallization in Kerr resonators suggests a new route for customizability of frequency-comb spectra and time-domain waveforms through engineering of mode interactions<sup>12,30</sup>. Additionally, our work and other theoretical work<sup>27</sup> suggests that it may be possible to use a mode crossing or a bichromatic pump to generate a seed crystal for creating complex, custom soliton trains, which could be populated through the use of a pulsed pump laser. This scheme presents a possible mechanism for chip-integrated optical data storage and manipulation. Finally, the mechanism we present here for soliton-soliton interactions has implications for periodic systems in any context in which nonlinearity and dispersion or diffraction contribute significantly to the dynamics.

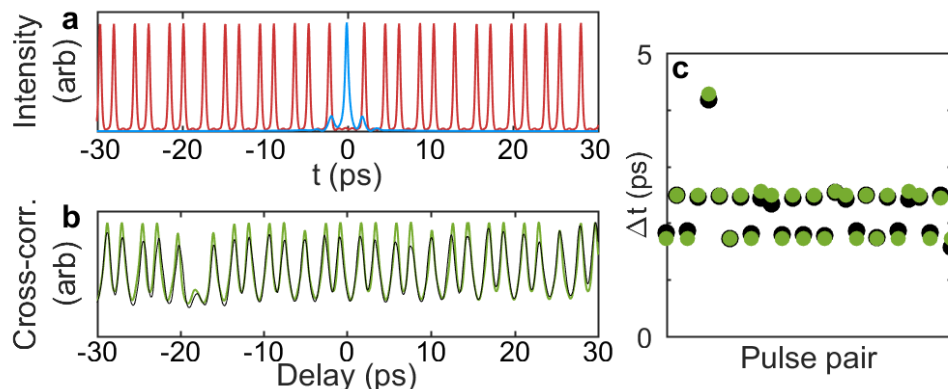


Figure 4. Intensity cross-correlation measurements of crystal (j) from Fig. 3. (a) Simulated crystal (red) and reference (blue) intensity profiles. (b) Measured (black) and simulated (green) cross-correlation signals. The contrast between peaks of the cross-correlation signal, for both theory and experiment, is limited by the duration and shape of the reference pulse, and increases between soliton pairs with larger temporal separations. (c) Temporal separations between adjacent peaks for the measured (black) and simulated (green) cross-correlation signals. Fractional error is 3.5 %.

## Methods

**Crystal generation:** Soliton crystals are generated in 16.4 GHz FSR disk<sup>31</sup> and 26 GHz FSR rod<sup>32</sup> silica resonators. The silica resonator has dispersion of  $\sim 10$  kHz/mode; the rod resonator is described in Ref. 24. For crystal generation, a telecom-wavelength pump laser (typically 1550–1565 nm) is coupled into a whispering-gallery mode of the resonator using a tapered optical fiber<sup>33</sup> and scanned with decreasing optical frequency across the resonance. A sawtooth-shaped frequency scan is used, with a period between 10 ms and 1 s. The scan range is typically on the order of 3 GHz, for scan rates from 3 to 300 GHz/s. Soliton crystals may also be generated by scanning the pump frequency arbitrarily slowly by hand. The pump laser's power is set to between 2.5 and 6 times the measured absolute threshold power for parametric oscillation, which typically results in 20–50 mW power input to the taper. To measure the optical spectrum of primary comb, chaos, or soliton crystal, the frequency scan is stopped at an appropriate point where the desired state exists. During the laser scan, the resonator absorbs laser power and heats up, which leads to an increase in the resonant wavelength due to thermo-optic effects that increase the optical path length. This results in a triangular, rather than Lorentzian, lineshape as the laser frequency is decreased<sup>25</sup>, a greatly increased resonant linewidth, and a hysteretic lineshape that is dependent upon the direction of the scan.

Diagnostics collected during crystal generation include the optical power transmitted through the tapered fiber, this same power with the pump frequency removed using a spatial-light modulator or optical band-reject filter, and the repetition-rate signal of the generated optical waveform collected by a 50 GHz photodiode.

Because crystal generation relies on a coupling between nominally orthogonal mode families in the resonator, it is sensitive to the position of the tapered optical fiber. The taper contacts the resonator and provides the coupling between mode families. The optimum taper position for crystal generation, in terms of position within the plane perpendicular to propagation and position along the taper's axis, is determined experimentally.

**Dynamical model:** Kerr comb generation is described by the Lugiato-Lefever equation<sup>19,34,35</sup>:

$$\frac{\partial \psi}{\partial \tau} = -(1 + i\alpha)\psi + i|\psi|^2\psi - i\frac{\beta}{2}\frac{\partial^2 \psi}{\partial \theta^2} + F. \quad (1)$$

Here  $\psi$  is the intracavity field, whose modulus is normalized to the threshold intracavity power<sup>19</sup> for parametric oscillation. The normalized time  $\tau$  is equal to  $t/2\tau_\gamma$ , where  $\tau_\gamma = 1/\Delta\omega$  is the resonator photon life-time. The pump detuning  $\alpha$  and the dispersion  $\beta$  are both normalized to half the resonance linewidth  $\Delta\omega$ :  $\alpha = -2(\omega_p - \omega_0)/\Delta\omega$ , where  $\omega_0$  is the angular frequency of the pumped resonance and  $\omega_p$  is the angular frequency of the pump laser;  $\beta = -2\xi_2/\Delta\omega$ , where  $\xi_2 = \left.\frac{\partial^2 \omega_\mu}{\partial \mu^2}\right|_{\mu=0}$ ,  $\omega_\mu$  being the angular frequency of the  $\mu^{\text{th}}$  resonator mode relative to the pumped mode, for which  $\mu = 0$ . The intracavity angular coordinate  $\theta$ , which ranges from 0 to  $2\pi$ , is measured in a frame which co-rotates at the group velocity of the pulses. The pump power  $F^2$  is normalized to the absolute threshold for parametric oscillation:  $F^2 = P_{\text{pump}}/P_{\text{threshold}}$ .

**Numerical simulations:** Numerical simulations are dynamic simulations of the Lugiato-Lefever equation via an adaptive<sup>36</sup> Runge-Kutta in the interaction picture<sup>37</sup> (RK4IP) method. This is a Fourier split-step method, in which the dispersion operator is applied in the frequency domain. Periodic boundary conditions are implicitly taken into account through the use of the fast Fourier transform algorithm and the specification of the intracavity field for one resonator round trip.

To simulate steady-state soliton crystals, initial conditions of the simulation must seed solitons in the appropriate locations, because solitons do not form spontaneously. Simulations of primary comb and chaos are run from zero initial intracavity field, and require the inclusion of simulated vacuum fluctuations. The simulated chaotic spectrum presented in Fig. 1c is a time-average, which is what is collected in the experiment due to the acquisition time of the optical spectrum analyzer—the chaotic spectrum varies on the time-scale of the photon life-time, as does the intracavity field, of which we have presented a simulated snapshot in Fig. 1d.

To perturb the LLE to account for the effect of a frequency shift of resonator modes due to a mode crossing, we note that it is possible to calculate the mode-dependent comb-resonator detuning  $\alpha_\mu = -2(\omega_p + \xi_1\mu - \omega_\mu)/\Delta\omega$ ,  $\xi_1$  being the FSR of the resonator at the pumped mode  $\xi_1 = \left.\frac{\partial \omega_\mu}{\partial \mu}\right|_{\mu=0}$ , by grouping together the pump-detuning term with the Fourier-transformed dispersion term:  $\alpha_\mu = \alpha - \beta\mu^2/2$ , where  $\beta < 0$  indicates anomalous dispersion and permits the formation of bright solitons. This formulation can be extended as necessary to include higher order dispersion, but we do not need to include higher-order dispersion in our simulations. Importantly, the formulation also permits inclusion of local changes in resonator mode structure through  $\delta$ -function perturbations of the comb-resonator detuning, in the form  $\alpha_\mu = \alpha - \frac{\beta\mu^2}{2} + \Delta\alpha_\mu$ ,  $\Delta\alpha_\mu$  being the normalized change in the frequency of the resonator mode:  $\Delta\alpha_\mu = 2(\omega_\mu - \omega_{\mu,o})/\Delta\omega$ .

In our implementation here, the LLE describes the evolution of the intracavity field. The experimental data we collect reflects the power spectrum of the field propagating away from the resonator in the tapered fiber, which includes through-coupled pump light. Thus, the relative amplitude of the pump laser with respect to the crystal is different for our experiments and our LLE simulations. We have corrected this by phenomenologically adjusting the pump laser power in the simulated optical spectrum to match the experimental data after the simulation is complete. In this way, we both account for the physical effect of the through-coupled pump and correctly simulate the soliton crystal dynamics, which the through-coupled pump does not affect.

**Simulation of soliton crystals:** The simulation of a soliton crystal exploits two independent experimental observations which are mutually confirmatory. First, the time-domain pulse train is deduced from the complicated shape of the optical spectrum of a soliton crystal by beginning with the assumption that the spectrum arises from a superposition of solitons, with no invocation of the crystallization theory we have presented above. A simple example is the pulse train corresponding to the “primary-comb-plus-soliton” spectrum in Fig. 1d, in which a soliton is added out of phase to a uniform soliton pulse train having a primary-comb-like spectrum. This soliton contributes the underlying single-FSR spectral envelope and eliminates a soliton from the pulse train in the time domain. Crystals with Frenkel defects may be understood in this way as well: the lobed structure in the spectrum is due to the spectral interference between an out-of-phase soliton which is added to the pulse train to remove a soliton, as above, and an in-phase soliton which is added to yield the shifted pulse.

Once the pulse train corresponding to the general structure of the spectrum has been deduced, the experimental spectrum can be compared to the spectrum of this pulse train calculated as a simple superposition of  $\text{sech}^2$  pulses. This comparison reveals excess power in the experimental spectrum, which is evidence of a mode crossing. The strength of the mode crossing, quantified by  $\Delta\alpha_{\mu_x}$ , is determined phenomenologically from the magnitude of the excess power, and reduced comb-resonator detuning on a single optical mode is incorporated into a perturbed LLE. It is then verified that the pulse train whose spectrum matches the experimental data is a steady-state solution to this perturbed LLE, which requires the inter-soliton separations to be multiples of the period of the beat between the excess power and the pump laser. This period is  $2\pi/\mu_x$ , where  $\mu_x$  is the mode-number where the comb-resonator detuning is reduced. This process connects the presence of excess power on a single optical mode of the spectrum to the general shape of the spectrum, two observations which a priori are not related.

This process is applied for all of the crystal states presented in Fig. 3 except for the disordered crystals and the crystal 3o. For 10 of the 13 experimental crystal spectra to which we apply the model the stabilizing mode crossing is visible in the data, although not necessarily shown in the figure; for the other three the position of the mode crossing is inferred from the distribution of solitons and other crystal states observed in the same resonator. To model the disordered crystals, the pulse train is not deduced from the shape of the optical spectrum. Instead, excess power due to a mode crossing is identified through the presence of an asymmetry in the spectrum about the pump. The location of the excess power then fixes the allowed inter-soliton separations in the resonator, after which an exhaustive search is performed until a pulse train is found that yields the experimental spectrum. As described in the text, we have not simulated spectrum 3o as a steady-state solution to any perturbed LLE, which we expect is because the crystal is stabilized by a more complex spectrum of excess power.

As can be seen in Fig. 3 in the main text, generally there is good agreement between simulated spectra of soliton crystals and the spectra we obtain in the experiment. It is possible to quantify this agreement by beginning from a crystallized pulse train and adjusting the pulse positions to minimize the error between experimental and calculated spectra. The difference between the pulse train which minimizes this error and the truly crystallized pulse train can then be calculated. When this procedure is performed, for example, for the “primary-comb-plus-soliton” crystal presented in Fig. 1 in the main text, the quadrature sum of the normalized differences in the inter-pulse spacing between the two pulse trains is 2.3 %.



**Instability of soliton crystals under the LLE:** None of the crystals we present are steady-state solutions to the unperturbed LLE. To arrive at this conclusion, we note that the temporal width of the pulses is determined by the bandwidth of the spectrum. This sets a lower bound on the range of their attractive interactions, which is too large for any of the crystals to be stable.

In Extended Data Fig. E1, we demonstrate the crystallization of an initially non-uniform pulse train due to the presence of a mode crossing, as well as the instability of the same pulse train without the mode crossing to stabilize it.

**Cross-correlation measurements:** Extended Data Fig. E2 presents a schematic depiction of the cross-correlation measurements, for which we use a commercial optical cross-correlator with a  $\text{LiIO}_3$  crystal. We use for a reference pulse the output of an electro-optic comb generator<sup>38</sup> whose repetition rate is locked to the repetition rate of the  $\sim 16.4$  GHz crystal pulse train and which is generated from the same pump laser. When the reference pulse and the soliton crystal pulse train are sent together into the nonlinear crystal exhibiting the  $\chi_2$  nonlinearity at  $90^\circ$  angles to each other, an amount of light proportional to the product of their intensities, at the sum of their frequencies, is emitted in a third direction. By measuring the average power of this emitted light while scanning the relative delay, we measure the intensity cross-correlation between the crystal and the reference pulse.

We operate our experiment in a through-coupled configuration, which results in destructive interference between the out-coupled solitons and the through-coupled pump. The solitons manifest as dips in the through-coupled intensity, resembling so-called dark solitons<sup>19</sup>. To correct this we use a spatial light modulator to adjust the phase and amplitude of the pump laser so that it constructively interferes with the solitons with maximal contrast.

The simulated cross-correlation signal is sensitive to the intensity profile of the reference pulse. We can measure only its intensity autocorrelation, which we combine with our knowledge of the method of its production to estimate the intensity profile. To demonstrate that the validity of the results we present here is not sensitive to the exact assumptions we make about the intensity profile, we have also simulated the intensity cross-correlation resulting from an assumed Gaussian reference pulse with the same autocorrelation width as is measured for the reference pulse. The resulting simulated cross-correlation does not qualitatively agree as well with the experimental data in the depths of the wells between peaks because it does not contain satellite pulses which contribute to the variations in this depth, but the quantitative comparison of the temporal spacing between peaks is similar: the mean (maximum) normalized error between experiment and theory is 3.5 % (9.1 %) for the assumed electro-optic comb pulse and 4.8 % (10.6 %) for the Gaussian pulse.

## References

1. Russell, J. S. Report on Waves. *Fourteenth Meet. Br. Assoc. Adv. Sci.* 311–390 (1844).
2. Lonngren, K. E. Soliton experiments in plasmas. *Plasma Phys.* **25**, 943–982 (1983).
3. Craig, W., Guyenne, P., Hammack, J., Henderson, D. & Sulem, C. Solitary water wave interactions. *Phys. Fluids* **18**, 57106 (2006).
4. Denschlag, J. *et al.* Generating Solitons by Phase Engineering of a Bose-Einstein Condensate. *Science* **287**, 97–101 (2000).
5. Akhmediev, N. & Ankiewicz, A. *Dissipative Solitons: From Optics to Biology and Medicine (Lecture Notes in Physics)*. (Springer, 2009).
6. Grelu, P. & Akhmediev, N. Dissipative solitons for mode-locked lasers. *Nat. Photonics* **6**, 84–92 (2012).
7. Kärtner, F. X. & Keller, U. Stabilization of solitonlike pulses with a slow saturable absorber. *Opt. Lett.* **20**, 16–18 (1995).
8. Hasegawa, A. & Tappert, F. Transmission of stationary nonlinear optical pulses in dispersive dielectric fibers. I. Anomalous dispersion. *Appl. Phys. Lett.* **23**, 171–172 (1973).
9. Haus, H. A. & Wong, W. S. Solitons in optical communications. *Rev. Mod. Phys.* **68**, 423–444 (1996).
10. Mollenauer, L. F., Stolen, R. H. & Gordon, J. P. Experimental observation of picosecond pulse narrowing and solitons in optical fibers. *Phys. Rev. Lett.* **45**, 1095–1098 (1980).

11. Herr, T. *et al.* Temporal solitons in optical microresonators. *Nat. Photonics* **8**, 145–152 (2014).
12. Herr, T. *et al.* Mode Spectrum and Temporal Soliton Formation in Optical Microresonators. *Phys. Rev. Lett.* **113**, 123901 (2014).
13. Joshi, C. *et al.* Thermally Controlled Comb Generation and Soliton Modelocking in Microresonators. *Opt. Lett.* **41**, 2565–2568 (2016).
14. Yi, X., Yang, Q.-F., Yang, K. Y., Suh, M.-G. & Vahala, K. Soliton frequency comb at microwave rates in a high-Q silica microresonator. *Optica* **2**, 1078–1085 (2015).
15. Kippenberg, T. J., Holzwarth, R. & Diddams, S. A. Microresonator-based optical frequency combs. *Science* **332**, 555–559 (2011).
16. Pfeifle, J. *et al.* Coherent terabit communications with microresonator Kerr frequency combs. *Nat. Photonics* **8**, 375–380 (2014).
17. Papp, S. B. *et al.* Microresonator frequency comb optical clock. *Optica* **1**, 10–14 (2014).
18. Diddams, S. A. The evolving optical frequency comb [Invited]. *J. Opt. Soc. Am. B* **27**, B51–B62 (2010).
19. Godey, C., Balakireva, I. V., Coillet, A. & Chembo, Y. K. Stability analysis of the spatiotemporal Lugiato-Lefever model for Kerr optical frequency combs in the anomalous and normal dispersion regimes. *Phys. Rev. A* **89**, 63814 (2014).
20. Yang, K. Y. *et al.* Broadband dispersion-engineered microresonator on a chip. *Nat. Photonics* **10**, 316–320 (2016).
21. Okawachi, Y. *et al.* Bandwidth shaping of microresonator-based frequency combs via dispersion engineering. *Opt. Lett.* **39**, 3535–3538 (2014).
22. Drake, T. E. *et al.* An octave-bandwidth Kerr optical frequency comb on a silicon chip. *Conf. Lasers Electro-Optics, Tech. Dig. STu3Q.4* (2016).
23. Del’Haye, P., Beha, K., Papp, S. B. & Diddams, S. A. Self-injection locking and phase-locked states in microresonator-based optical frequency combs. *Phys. Rev. Lett.* **112**, 43905 (2014).
24. Del’Haye, P. *et al.* Phase steps and resonator detuning measurements in microresonator frequency combs. *Nat. Commun.* **6**, 5668 (2015).
25. Carmon, T., Yang, L. & Vahala, K. J. Dynamical thermal behavior and thermal self-stability of microcavities. *Opt. Express* **12**, 4742–4750 (2004).
26. Herr, T. *et al.* Universal formation dynamics and noise of Kerr-frequency combs in microresonators. *Nat. Photonics* **6**, 480–487 (2012).
27. Hansson, T. & Wabnitz, S. Bichromatically pumped microresonator frequency combs. *Phys. Rev. A* **90**, 13811 (2014).
28. Haus, H. A. & Huang, W. Coupled-Mode Theory. *Proc. IEEE* **79**, 1505–1518 (1991).
29. Weiner, A. *Ultrafast Optics*. (Wiley, 2009).
30. Liu, Y. *et al.* Investigation of mode coupling in normal-dispersion silicon nitride microresonators for Kerr frequency comb generation. *Optica* **1**, 137–144 (2014).
31. Lee, H. *et al.* Chemically etched ultrahigh-Q wedge-resonator on a silicon chip. *Nat. Photonics* **6**, 369–373 (2012).
32. Del’Haye, P., Diddams, S. A. & Papp, S. B. Laser-machined ultra-high-Q microrod resonators for nonlinear optics. *Appl. Phys. Lett.* **102**, 221119 (2013).
33. Spillane, S. M., Kippenberg, T. J., Painter, O. J. & Vahala, K. J. Ideality in a fiber-taper-coupled microresonator system for application to cavity quantum electrodynamics. *Phys. Rev. Lett.* **91**, 43902 (2003).
34. Chembo, Y. K. & Menyuk, C. R. Spatiotemporal Lugiato-Lefever formalism for Kerr-comb generation in whispering-gallery-mode resonators. *Phys. Rev. A* **87**, 53852 (2013).
35. Coen, S., Randle, H. G., Sylvestre, T. & Erkintalo, M. Modeling of octave-spanning Kerr frequency combs using a generalized mean-field Lugiato-Lefever model. *Opt. Lett.* **38**, 37–39 (2013).
36. Sinkin, O. V., Holzlöhner, R., Zweck, J. & Menyuk, C. R. Optimization of the split-step Fourier method in modeling optical-fiber communications systems. *J. Light. Technol.* **21**, 61–68 (2003).
37. Hult, J. A Fourth-Order Runge-Kutta in the Interaction Picture Method for Simulating Supercontinuum Generation in Optical Fibers. *J. Light. Technol.* **25**, 3770–3775 (2007).
38. Beha, K. *et al.* Self-referencing a continuous-wave laser with electro-optic modulation. *arXiv: 1507.06344*

(2015).

### Supplementary Information

**Phase steps:** Soliton crystals exhibit phase steps previously reported by Del’Haye et al<sup>24</sup>. We plot simulations of several crystals with spectral phase in Extended Data Fig. E3. We note that, because a linear spectral phase shift is equivalent to a shift in time, there is an infinite continuum of ways to present the spectral phase for a given crystal, and they may not appear equivalent. The phase steps exhibited by soliton crystals arise due to the superposed linear spectral phase shifts from temporally-separated co-propagating solitons.

**Harmonic mode-locking:** We have compared and contrasted soliton ensembles in the tightly-packed and sparsely-populated regimes in the main text. In conducting numerical simulations, we have also observed harmonic mode-locking in Kerr combs. Harmonic mode-locking consists of the generation of a uniform soliton train, and occurs in a density regime between the regimes discussed in the text. In simulations, soliton ensembles in this density regime which are initialized with non-uniform soliton distributions will evolve to uniformity, with a spectrum resembling primary comb. Harmonic mode-locking does not require the presence of a mode crossing, and the harmonic mode-locking we have observed involves only the evolution towards a uniform pulse train; no other crystal structure has been discovered. Harmonic mode-locking is a weak effect: the timescale over which a non-uniform pulse distribution will evolve to uniformity in the case of harmonic mode-locking is on the scale of  $10^3$ – $10^5$  photon lifetimes, compared with  $<10$  photon lifetimes for crystallization of a non-uniform pulse train under the influence of a mode crossing. In Extended Data Fig. E4 we present simulations of harmonic mode-locking beginning from a uniform pulse train with jittered pulse positions, and beginning from a uniform pulse train with a vacancy. The numbers of solitons in these harmonically mode-locked states are 15 and 14, respectively; the simulation is conducted under the same conditions in which we have experimentally observed crystallization with 23 pulses in the presence of a mode crossing.

### Extended Data

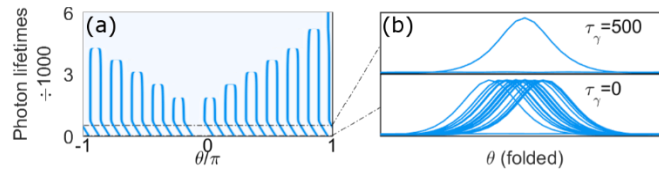


Fig. E1. (a) Simulated evolution of the pulse train corresponding to the experimental crystal spectrum shown in Fig. 1, starting from irregular pulse positions. Crystallization occurs within 10 photon-lifetimes of the initialization of the simulation. While the propagation is governed by a perturbed LLE including reduced comb-resonator detuning on modes  $5 \times 24=120$  and  $7 \times 24=168$ , from initialization to 500 photon lifetimes, the crystal drifts within the co-rotating frame because the optical spectrum is asymmetric. After the perturbation is removed smoothly from 500 to 1000 photon lifetimes, the pulses pair-annihilate, demonstrating that the mode crossing is critical for stabilizing the soliton crystal. (b) Intracavity power with the angular coordinate folded modulo  $2\pi/24$ , to illustrate the irregularity of the pulse positions at the initialization of the simulation and the crystallized pulse train at 500 photon lifetimes.

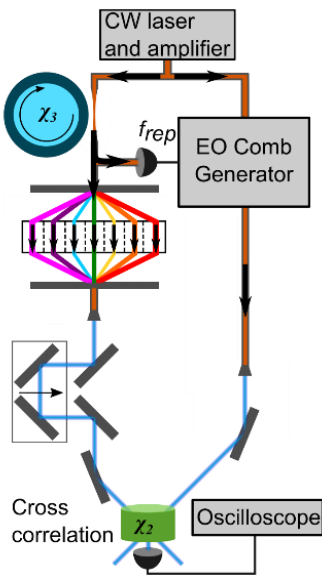


Fig. E2. Schematic depiction of the set-up for using an electro-optic (EO) modulator comb as a reference pulse to measure the time-domain waveform of the crystal. The  $\chi_3$  (Kerr) and  $\chi_2$  nonlinearities are indicated on the resonator and nonlinear crystal, respectively. A spatial-light modulator is used to rotate the phase of the crystal's pump laser by  $\pi$  and attenuate it by 3-4 dB to improve the cross-correlation contrast. The soliton crystal and the EO modulator comb share a pump laser, and the repetition frequency  $f_{\text{rep}}$  of the EO modulator comb is locked to that of the crystal. Varying the relative delay in one arm of the interferometer allows a measurement of the intensity cross-correlation between the crystal and the reference pulse.

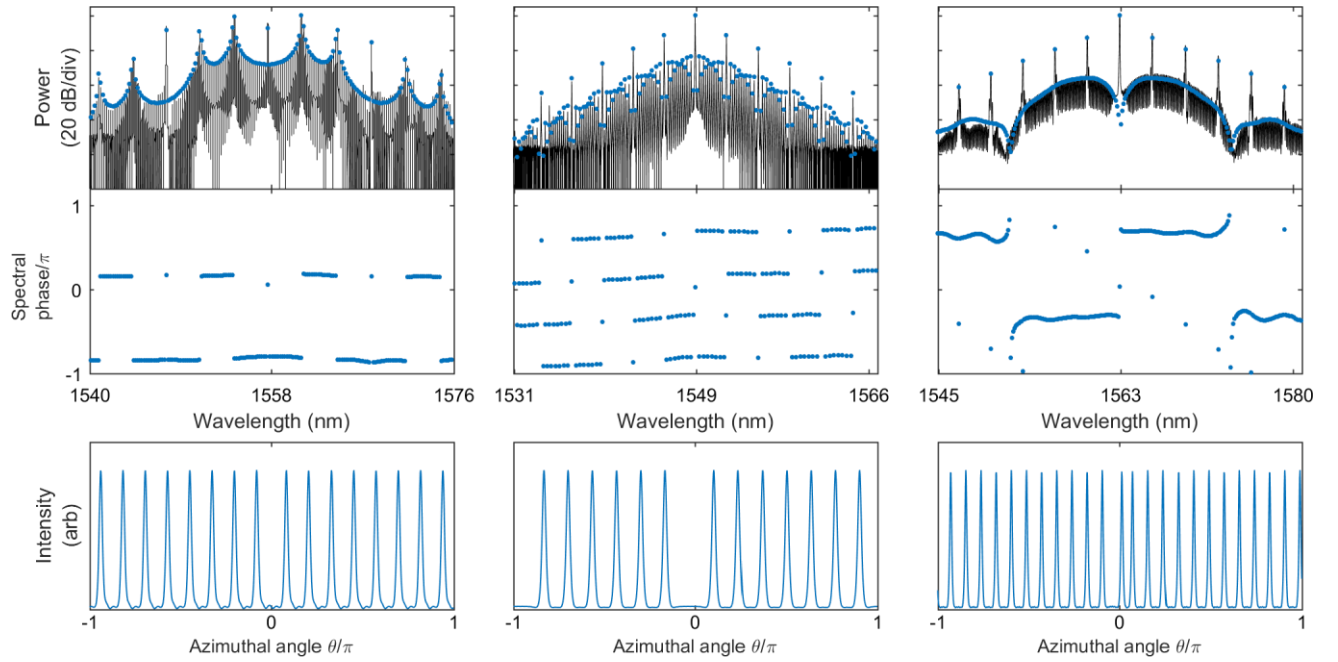


Fig E3. Depiction of crystals (p), (d), and (g) from Fig. 3 of the main text, with experimental data in black and simulations in blue, including simulated spectral phase. These crystals exhibit phase steps near prominent features of the spectrum, which arise due to the spectral interference between temporally-shifted solitons. Spectral phase is unique only up to a shift linear in frequency, which can yield multiple phase profiles for the same crystal which appear very different.

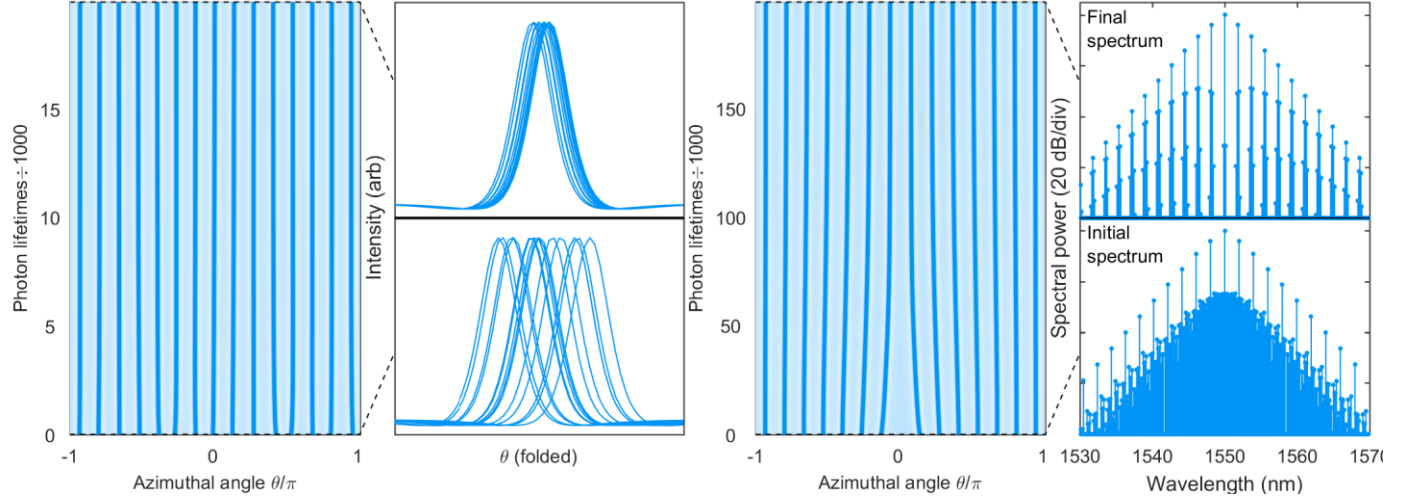


Fig E4. Simulations of harmonic mode-locking, or the evolution towards a uniform soliton train without the presence of a mode crossing. Left: Harmonic mode-locking of 15 pulses beginning from jittered, non-uniform pulse positions. Initial and final pulse configurations are shown with the angular coordinate folded modulo  $2\pi/15$  to illustrate the degree of regularity of the pulse distribution. The pulse distribution evolves towards a uniform pulse train, but approaches that distribution slowly. Right: Harmonic mode-locking of 14 pulses beginning from a uniform 15-soliton pulse train with a single vacancy.

### Acknowledgements

We thank Daniel Hickstein and Kyle Beloy for comments on the manuscript, and Ki Youl Yang and Kerry Vahala for providing the 16 GHz disk resonators. This material is based upon work supported by the Air Force Office of Scientific Research under award number FA9550-16-1-0016. Additional support is provided by the NIST-on-a-Chip program and the DARPA QuASAR and PULSE programs. DC acknowledges support from the NSF GRFP under Grant No. DGE 1144083. This work is a contribution of the US government and is not subject to copyright in the United States of America.

### Author Contributions

E.L., D.C., P.D.'H., and S. P. performed the crystal generation experiments. D.C. analyzed the data, developed the model, and performed the numerical simulations. E.L. performed the cross-correlation experiments. D.C. wrote the manuscript. All authors discussed the experiments and the model and contributed to revision of the manuscript.